# A Numerical Study of Correlation between Recirculation Length and Shedding Frequency in Vortex Shedding Phenomena

CARLO CRAVERO, NICOLA MAROGNA, DAVIDE MARSANO
Dipartimento di Ingegneria Meccanica, Energetica, Gestionale e dei Trasporti (DIME)
Università degli Studi di Genova
Via Montallegro 1 - 16145 Genova
ITALY

*Abstract:* The purpose of this paper is to characterize and to estimate the recirculating length behind an aerodynamic profile in ground effect with Gurney Flap. The flow characterization at high Reynolds numbers was performed by means of numerical analysis. A correlation between the size of the recirculation length and the frequency of vortex shedding was studied. The vortex shedding has a characteristic frequency, which, in this work, is correlated to the size of a recirculation length defined by the authors. The numerical investigation methodology applied to the profile with Gurney Flap, was previously developed on the well-documented test case of the flow around a cylinder at high Reynolds. The case was chosen to investigate and to validate the numerical approach with experimental data.

*Key-Words:* bluff bodies, CFD, vortex shedding, Gurney flap

Received: January 18, 2021. Revised: February 20, 2021. Accepted: March 3, 2021.
Published: March 5, 2021.

## 1 Introduction

The wake behind 2D and 3D bluff bodies has been a topic of interest for engineers over many years but it still remains a difficult case for both experimental and numerical applications. The wake structure is very complex, due to the interaction of three different layers: boundary layer, shear layer and the wake. Numerical and experimental investigations were carried to understand the flow mechanisms of the vortex shedding phenomenon that leads to high pressure fluctuations causing structural vibrations. Classical studies have been performed on the frequency of vortex shedding by Strouhal [1] and Rayleigh [2], according to various Reynolds numbers. Subsequently a remarkable impulse to understand the phenomenon was given by Theodore von Karman [3], who analyzed the stability at various wakes configurations at different Reynolds numbers. The above studies suggested correlations between the structures of the vortex and the drag on the profile. In this paper the von Karman vortex shedding is studied in two cases: a cylinder and a profile with Gurney Flap in ground effect. The flow around the 2D cylinder is an industrial problem concerning some applications such as offshore platform, power lines, bridge and heat exchangers. In the cylinder case four main flow regions can be identified, as shown in Figure 1.

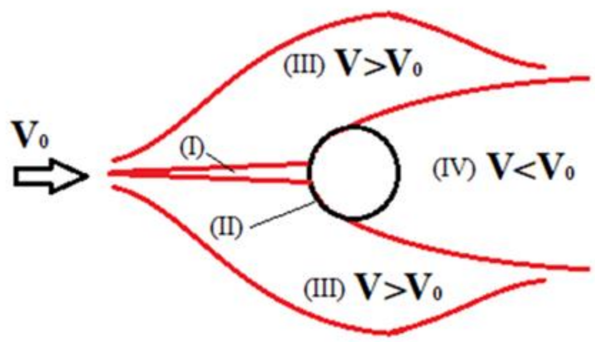


Figure 1. Main flow regions around cylinder merged in a flow at certain Reynolds number

Upstream the cylinder a stagnation zone (i) where the flow is slowed down to zero at the point of contact next to the cylinder. After the stagnation point up and down, areas of accelerated flow (compared to incident flow velocity of the incident vein) are observed (iii). A thin region adherent to the cylinder, called boundary layer (ii), flows into the final zone called wake (iv) where flow adherence to the wall is lost.

Gerrard [4] published an important review about the flow region near the back of the cylinder that plays a key role in determining the frequency of the vortex shedding. The main variations in the wake region are observed in the Reynolds number range $10^3$ to $5x10^5$ where the so-called drag crisis is observed [5]. The recirculation zone in the wake (recirculation bubble) is experimentally defined as the region where the streamwise velocity component is negative. At the end of the recirculation zone, behind the cylinder along the centerline, there is a certain point where the external fluid in the shear layer first goes across this line. It has been observed that changes in Reynolds number affect recirculation zone size: by increasing it, the instability intensity leading to the shear layer curl (the formation of the first vortex that draws the separate fluid layer on the opposite side) increases. Regarding the formation time of finite whirl, due to the phenomenon previously described, is reduced and vortex shedding frequency increases [6, 7]. Considerable variation in Pressure Coefficient ($Cp_b$) has been observed with Reynolds number; it is sensitive to a variation due to flow instability changes and phenomena that occur into the range of Reynolds numbers considered.

Results obtained from studies and experiments [8] on the $Cp_b$ values showed that behind the cylinder (close to the recirculating bubble) there is a minimum of the pressure coefficient measured from the base suction point. Extensive aerodynamic analysis on the profile in ground effect has been performed and the effect of the Gurney Flap on the flow unsteadiness has been discussed [9].

According to the above experience a correlation between shedding frequency and the size of the recirculation bubble (i.e. length along centerline) has been developed. The Gurney Flap [10], introduced in racing cars by the driver and constructor Daniel Gurney, is a simple device consisting of a small metal strip, mounted perpendicular in the trailing edge on the pressure suction of an aerodynamic profile. An aerodynamic study [11] was carried out in a wind tunnel on a racing car spoiler with a flap height of 1.25% of the profile chord.

The results of this study led to the conclusion that this device modifies the Kutta-Joukowski condition for a wing profile operating under subsonic conditions. This condition requires that the flow from both surfaces mix in the wake, referring to Figure 2, the stagnation point (S2) moves to the trailing edge (because of the shorter distance ran by point B), creating an anti-clockwise vortex.

As a direct consequence for the Kelvin-Helmholtz theorem on vorticity, the entire system will respond by creating a vortex with opposite vorticity.

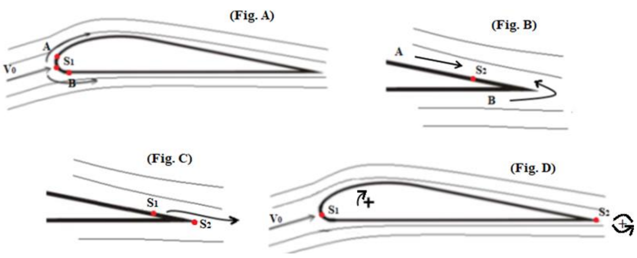


Figure 2. Theory about flow around a wing, Circulation Theorem regions

Based on theory and on experimental data available, the hypothesis from these studies highlights a small separate flow region directly upstream of the Gurney and two counter rotating vortices downstream, sketched in Figure 3, which have a rotational effect on the local flow field. The result is an increase of the circulation, hence an increase in downforce from the profile. A further beneficial effect [11] is that the delayed separation of the suction stream increases the operating range of the profile at higher angle of attack before stall. Higher aerodynamic load and increased aerodynamic efficiency can be obtained. The spectral analysis of the LDA signal [12] clearly showed that the instantaneous flow behind the profile consists in a swirling wake with alternate vortices.

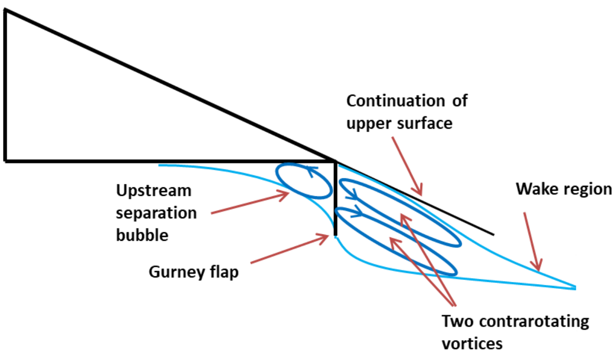


Figure 3. Recirculation bubbles and steady vortices around Gurney flap

The unsteady CFD approach considered has showed its ability to efficiently predict the unsteady vortex shedding from bluff bodies with engineering accuracy; it can be used for design/analysis of components [9,13,14] or for tonal noise prediction [15]. The purpose of this paper is to develop a methodology that allows to quantitatively predict the recirculation bubble length in the area downstream of a bluff body and to correlate it with the vortex shedding frequency. As regards 2D cases have been adopted

## 2 Basic equations: flow model

In a two dimensional flow the Reynolds-averaged equations for conservation of mass and momentum are:

$$\frac{\partial \rho}{\partial t} + \frac{\partial}{\partial x_j}\left(\rho u_j\right) = 0 \tag{1}$$

$$\frac{\partial \rho u_i}{\partial t} + \frac{\partial}{\partial x_j}\left(\rho u_i u_j\right) = -\left(\frac{\partial P}{\partial x_i}\right) + \frac{\partial}{\partial x_j}\left[\mu_{eff}\left(\frac{\partial u_i}{\partial x_j} + \frac{\partial u_j}{\partial x_i}\right)\right] + S_M \tag{2}$$

where i,j = 1, 2. Here $x_1$ and $x_2$ denote the horizontal and vertical directions, respectively; $u_1$ and $u_2$ are the corresponding mean velocity components; $S_M$ is the sum of body force; P is the dynamic pressure; ρ is the density of the fluid; and $\mu_{eff}$ is the effective viscosity accounting for turbulence, defined as follows:

$$\mu_{eff} = \mu + \mu_t \tag{3}$$

where $\mu_t$ is the turbulence viscosity, modeled according the appropriate turbulence model.

This study assumes 2D flow around bluff bodies and literature have shown that 2D computation can over-estimate the forces acting on the body (Benim et al. [16]; Liuliu et al. [17]).

However, the intention of this study is to to develop a methodology to quantitatively predict the recirculation length downstream of a bluff body and to correlate it with the vortex shedding frequency. 2D cases can be effective for the scope with a considerable saving of computational resources.

### 2.1 Transport equations for the Standard k-ε model

A standard high Reynolds number k-ε is used in the present study [18,19]. This model has been applied on vortex shedding by previous works [20]. The k and ε equations are given by:

$$\frac{\partial}{\partial t}(\rho k) + \frac{\partial}{\partial x_i}(\rho k u_i) = \frac{\partial}{\partial x_j}\left[\left(\mu + \frac{\mu_t}{\sigma_k}\right)\frac{\partial k}{\partial x_j}\right] + G_k + G_b - \rho\varepsilon - Y_M + S_k \tag{4}$$

$$\frac{\partial}{\partial t}(\rho \varepsilon) + \frac{\partial}{\partial x_i}(\rho \varepsilon u_i) = \frac{\partial}{\partial x_j}\left[\left(\mu + \frac{\mu_t}{\sigma_\varepsilon}\right)\frac{\partial \varepsilon}{\partial x_j}\right] + C_{1\varepsilon}\frac{\varepsilon}{k}(G_k + C_{3\varepsilon}G_b) - C_{2\varepsilon}\rho\frac{\varepsilon^2}{k} + S_\varepsilon \tag{5}$$

In these equations, $G_k$ represents the generation of turbulent kinetic energy due to the mean velocity gradients; $G_b$ is the generation of turbulent kinetic energy, due to buoyancy; $Y_M$ represents the contribution of the fluctuating dilatation in compressible turbulence to the overall dissipation rate; while $S_k$ and $S_\varepsilon$ are source terms. The turbulent (or eddy) viscosity $\mu_t$ is computed by combining k and ε:

$$\mu_t = \rho C_\mu \frac{k^2}{\varepsilon} \tag{6}$$

The following standard model coefficients have been adopted: $C_{1\varepsilon}$=1.44, $C_{2\varepsilon}$=1.92, $C_\mu$=0.09, $\sigma_k$=1.0 $\sigma_\varepsilon$=1.3.

### 2.2 Transport equations for the (SST) k-ω model

The SST model is based on the baseline (BSL) k-ω turbulence model, combining the equations of ε and ω with a blending factor [21]. This blending factor is based on the local a-dimensional wall distance Y+ that switches the model from a k-ω near the walls to a k-ε in the free shear flows. The (BSL) k-ω model has a similar two-equation form as the k-ε model. The transport equations for the model are:

$$\frac{\partial}{\partial t}(\rho k) + \frac{\partial}{\partial x_i}(\rho k u_i) = \frac{\partial}{\partial x_j}\left[\left(\mu + \frac{\mu_t}{\sigma_k}\right)\frac{\partial k}{\partial x_j}\right] + G_k - Y_k + S_k \tag{7}$$

$$\frac{\partial}{\partial t}(\rho \omega) + \frac{\partial}{\partial x_j}(\rho \omega u_j) = \frac{\partial}{\partial x_j}\left[\left(\mu + \frac{\mu_t}{\sigma_\omega}\right)\frac{\partial \omega}{\partial x_j}\right] + G_\omega - Y_\omega + D_\omega + S_\omega \tag{8}$$

with:

$$\mu_t = \alpha^* \frac{\rho k}{\omega} \tag{9}$$

where α* is a correction factor for low-Reynolds, while $G_\omega$ represents the generation of ω; $Y_k$ and $Y_\omega$

represent the dissipation of k and ω due to turbulence; $D_\omega$ represents the cross-diffusion term; $S_k$ and $S_\omega$ are source terms. All these terms, the blending factors and their respective model constants are reported in [21].

### 2.3 Transition model γ-θ

The transition model γ-θ is based on the coupling of the SST k-ω transport equations with two other transport equations. For the intermittency γ the transport equation is defined as:

$$\frac{\partial(\rho\gamma)}{\partial t}+u_j\frac{\partial(\rho u\gamma)}{\partial x_j} = P_{\gamma 1}-E_{\gamma 1}+P_{\gamma 2}-E_{\gamma 2} + \frac{\partial}{\partial x_j}\left[\left(\mu+\frac{\mu_T}{\sigma_\gamma}\right)\frac{\partial\gamma}{\partial x_j}\right] \quad (10)$$

The transition sources are defined as follows:

$$P_{\gamma 1} = C_{a1}F_{lenght}\rho S[\gamma F_{onset}]^{C_{\gamma 3}} \quad (11)$$

$$E_{\gamma 1} = C_{e1}P_{\gamma 1}\gamma \quad (12)$$

where S is the strain rate magnitude, $F_{lenght}$ is an empirical correlation that controls the length of the transition region, while $C_{a1}$ and $C_{e1}$ hold the values of 2 and 1 respectively. Then the destruction/relaminarization sources are defined as follows:

$$P_{\gamma 2} = C_{a2}\rho\Omega\gamma F_{turb} \quad (13)$$

$$E_{\gamma 2} = C_{e2}P_{\gamma 2}\gamma \quad (14)$$

where Ω is the vorticity magnitude, while the other constants for the intermittency equation are: $C_{a2}$=0.06, $C_{e2}$=50, $C_{\gamma 3}$=0.5, $\sigma_\gamma$=1.0. The transition onset is controlled by the function reported in [21]. The transport equation for the transition momentum thickness Reynolds number $\widetilde{Re_{\theta t}}$ is:

$$\frac{\partial(\rho\widetilde{Re_{\theta t}})}{\partial t}+u_j\frac{\partial(\rho u_j\widetilde{Re_{\theta t}})}{\partial x_j} = P_{\theta t}+\frac{\partial}{\partial x_j}\left[\sigma_{\theta t}(\mu+\mu_T)\frac{\partial\widetilde{Re_{\theta t}}}{\partial x_j}\right] \quad (15)$$

The source term is defined as follows:

$$P_{\theta t} = C_{\theta t}\frac{\rho^2u^2}{500\mu}(Re_{\theta t}\widetilde{Re_{\theta t}})(1.0-F_{\theta t}) \quad (16)$$

The model constants for the $\widetilde{Re_{\theta t}}$ equation are: $C_{\theta t}$=0.03, $\sigma_{\theta t}$=2.0; the expressions for the constant $F_{\theta t}$ are reported in [21].

## 3 Flow around cylinder at high Reynolds numbers

A well-documented case from literature is chosen as preliminary case: a 2D cylinder in uniform flow at high Reynolds number with vortex shedding. The Ansys CFD platform is used to solve the flow model based on RANS equations with k-ε turbulent model and γ-θ transition model (only when the transition is considered), described in the previous section. The unsteady simulations have been performed in Reynold's similarity in the range between $1x10^6$ and $3.6x10^6$. Reference values for the computational domain size and boundary conditions have been taken from ref. 10. A rectangular domain is suitable to capture the Von Karman vortex: it extends 7D upstream of the cylinder (D = 0.2 m), 20D downstream and 7D each side. Figure 4 shows both domain and mesh details. A structured grid is generated with y+ close to one at the cylinder wall.

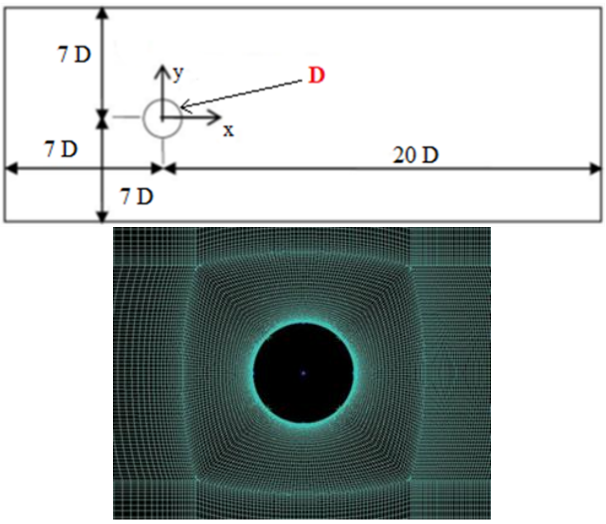


Figure 4. Domain size scheme and structured mesh grid detail.

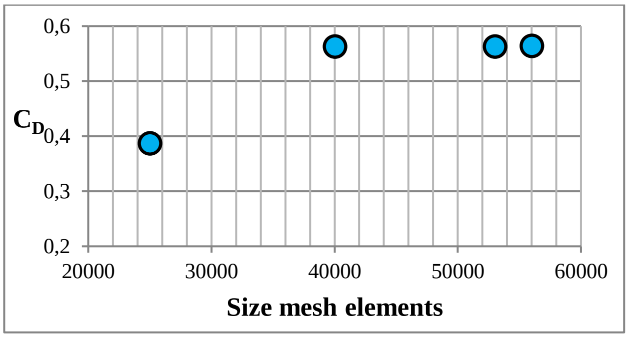


Figure 5. Grid Dependency, Sensitivity analysis

DOI: 10.37394/232013.2021.16.6


A sensitivity analysis was performed for the number of grid elements and Figure 5 shows the drag coefficient trend with the mesh. The drag coefficient has been defined as:

$$C_D = \frac{D_R}{\frac{1}{2}\rho A U^2} \tag{17}$$

A mesh size of about 50 000 has been selected. The unsteady analysis are initialized with a steady run with inlet uniform axial velocity $U_\infty$ = 73.5 [m/s] (Re = $10^6$) or $U_\infty$ = 264.5 [m/s] (Re =$3.6\times10^6$). A turbulence intensity I=0.8% is set at the inlet. Slip boundary condition for lateral domain boundaries is set. Free outflow condition is fixed at the outlet. For the unsteady simulations a time step $\Delta t$= $4{,}082x10^{-5}$ [s] is fixed according to the Courant condition. A second order SIMPLE solution scheme is adopted.

### 3.1 Drag coefficient and Strouhal number

The experimental work from ref. [22] with hot-wire analysis is considered as reference. Table 1 compares the $C_D$ values obtained from CFD analysis. Figure 6 shows the variation of $C_D$ with Reynolds number, and compares experimental and numerical data.

Table 1. Drag Coefficient comparison ($C_D$).

| Study case | $C_D$ (Re=$1\times10^6$) | $C_D$ (Re=$3.6\times10^6$) |
|---|---|---|
| 2D URANS k-ε | 0.564 | 0.565 |
| 2D URANS (Transition γ-θ) | 0.625 | 0.573 |
| Ong et al. 2D URANS k-ε [20] | 0.517 | 0.457 |
| Roshko [22] | 0.21 – 0.63 | 0.36 – 0.75 |

The Strouhal number:

$$St = \frac{fD}{U_\infty} \tag{18}$$

is shown in Figure 7 where the data from literature are compared to the values obtained in the present work.

A good agreement between numerical 2D simulations and experimental data is observed. For Reynolds numbers lower than $10^6$ the reattaching is not symmetrical, the wake is distorted, there is a drag drop and the shedding phenomenon disappears. In all simulations performed the periodic phenomenon is present as shown in Figure 8 (instantaneous snapshot of velocity contours). In the supercritical region $C_D$ increases from 0.3 to 0.7. For Re higher than $10^6$ a wall separation bubble appears and the numerical transition model has been useful to solve this phenomenon attached to the wall. A comparison for Strouhal number at different Reynolds regimes is showed in Table 2 and Figure 7. The vorticity contours of Figure 9 help to highlight the vortex shedding phenomena.

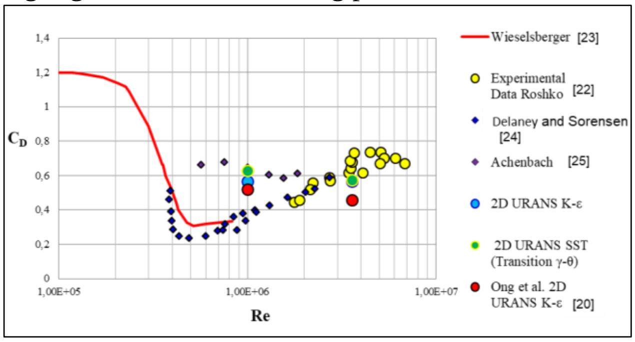


Figure 6. Drag Coefficient vs Reynolds number

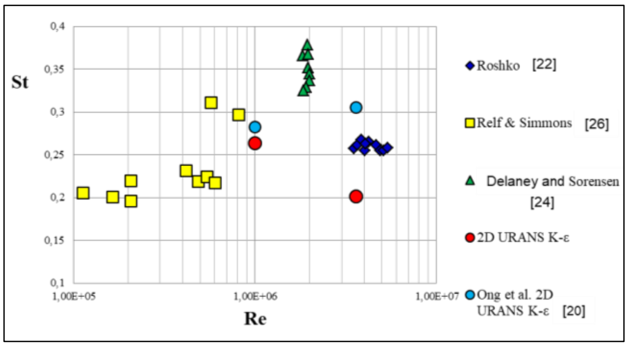


Figure 7. Strouhal number vs Reynolds number

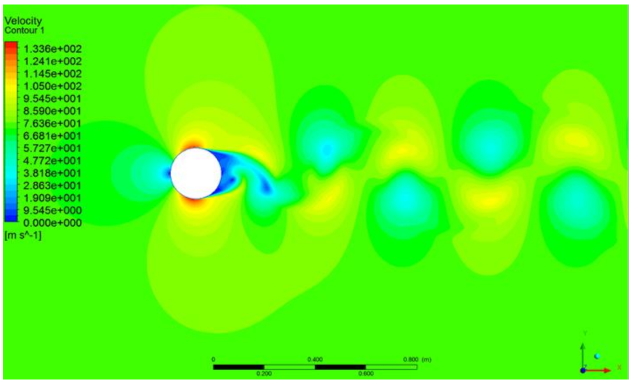


Figure 8. Velocity contour into the domain at Re =$1\times10^6$

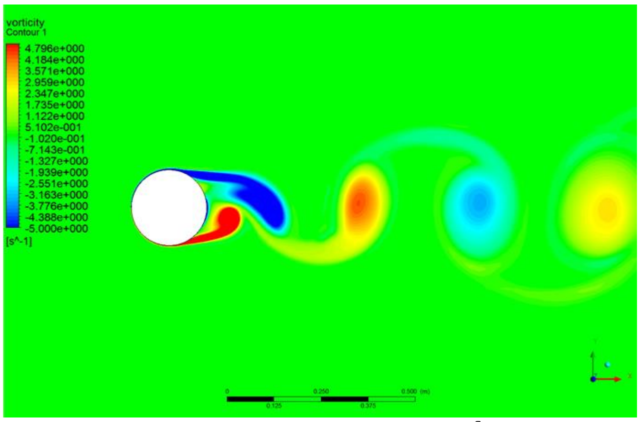


Figure 9. Vorticity contour at Re =$1\times10^6$

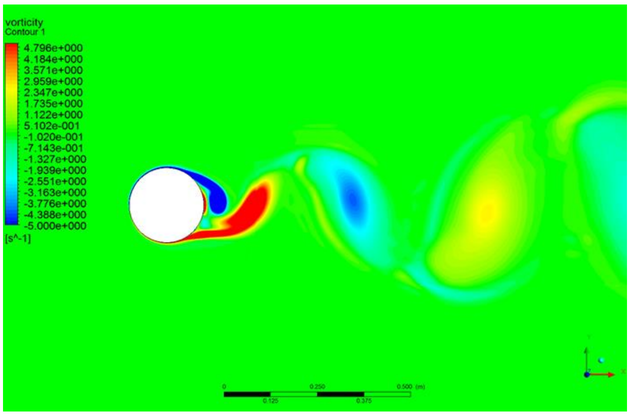

Figure 10. Vorticity contour at Re =3.6×10$^6$

Table 2. Drag Coefficient comparison ($C_D$)

| Study case | St (Re=1×10⁶) | St (Re=3.6×10⁶) |
|---|---|---|
| 2D URANS k-ε | 0.263 | 0.201 |
| Ong et al. 2D URANS k-ε [20] | 0.2821 | 0.305 |
| Roshko [22] | 0.18 – 0.50 | 0.17 – 0.29 |

### 3.2 Pressure Coefficient

The numerical approach is able to predict the alternate vortex shedding in the supercritical regime (Re $1x10^6$). At this Reynolds number, as previously mentioned, a non-symmetrical recirculating bubble at the cylinder wall induces an asymmetrical vortex shedding. The above detail has not been captured by the experimental investigations. In order to have a deeper insight into the flow mechanism at the wall region the pressure coefficient distributions are discussed. The local instantaneous pressure coefficient is:

$$C_p = \frac{p - p_\infty}{\frac{1}{2}\rho_\infty U_\infty^2} \tag{19}$$

The time average pressure coefficient is computed with averaged local pressure values on a single period T of the unsteady shedding. The obtained distributions are compared with experimental data in Figure 11-12 for Re=10$^6$ and Re=3.6×10$^6$ respectively. The values of the base suction coefficient ($C_p$ at 180° from the stagnation point) are reported in Table 3. A good agreement is obtained apart from the region behind the cylinder where a boundary layer transition occurs. At Re=10$^6$ the transition in the boundary layer generates a recirculating area at the wall where the $C_p$ distribution has a kink. Laminar separation and turbulent reattachment lead the flow to separate at very high angle around the cylinder from the stagnation point. The following regions in the Re range are distinguished (the angle θ start in clockwise from stagnation point): the subcritical region (vortex shedding and laminar separation at $\theta_s$<90°), the critical region (vortex shedding disappears, the reattachment is asymmetrical for $\theta_s$>90° and the wake is broken), supercritical region for Re>10$^6$. In this last region the transition moves from the shear layer to the wall boundary layer. At the upper limit of the critical region a recirculation bubble at the wall appears that moves the turbulent separation point of the wake at high downstream angle. Increasing the Re from the critical region the observed sequence is: a laminar separation, turbulent reattachment, and turbulent separation of the boundary layer. The recirculating bubble reduces increasing Reynolds number for Re>1.5×10$^6$ and it is not observed beyond this flow regime [25]. At Re = 3.6×10$^6$ there is no further separation and the recirculating bubble disappears.

Table 3. $Cp_b$ comparison

| Study case | $Cp_b$ (Re=1×10⁶) | $Cp_b$ (Re=3.6×10⁶) |
|---|---|---|
| 2D URANS k-ε | -0.699 | -0.779 |
| 2D URANS (Transition γ-θ) | -1.165 | -0.947 |
| Ong et al. 2D URANS k-ε [20] | -0.601 | -0.546 |
| Achenbach [25] | -0.442 (Re=8.5$x$10⁵) | -0.826 |

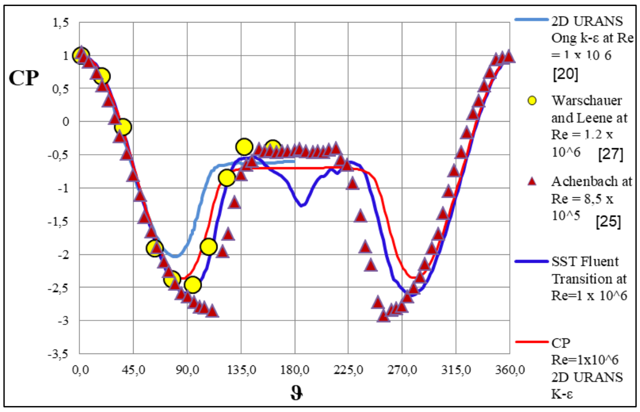


Figure 11. Pressure coefficient comparison at Re=10$^6$

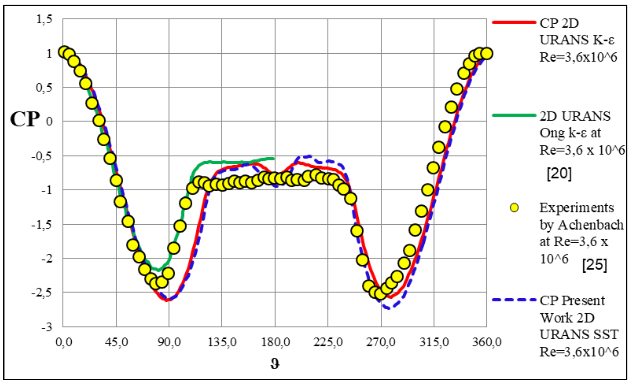

Figure 12. Pressure coefficient comparison at $Re=3.6\times10^6$

### 3.3 Skin Friction Coefficient

In order to better understand the flow condition at the wall and to identify the separated zone, the skin fraction coefficient has been studied. In Table 4, the obtained numerical values are plotted and in Figure 13 and 14 the trends for two flow regimes are compared with other numerical results [20,28]. The different results are in good agreement each other. Figure 13 at $Re=1x10^6$ shows that the numerical transition model is able to predict the actual trend described in literature [20], except for the recirculating bubble that has been observed only numerically. The transition model shows flow condition at the wall where there is transition in boundary layer after reattachment of laminar recirculating bubble (depicted in the detail of Figure 16). For $Re=3.6x10^6$ Figure 14 highlights a good agreement between all the numerical results. The transition model shows that, from one certain angle the wall stress increases (with respect to the other cases predicted using other models) where the occurrence of wall transition in the boundary layer from laminar to turbulent flow regime is locally detected. No laminar recirculation bubble at the wall is detected for this Re and symmetrical turbulent vortex shedding starts at this regime, called Super-critical or Post-Critical. In Figure 15 the contours of the Intermittency value obtained from the activation of the transition model show the wall laminar and turbulent flow to detect the boundary layer transition zone.

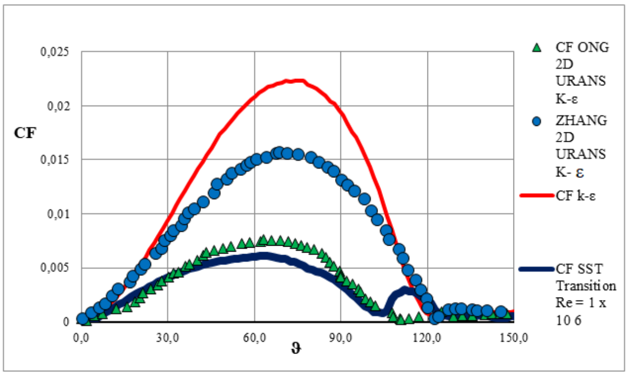


Figure 13. Skin friction factor comparison at $Re=1x10^6$

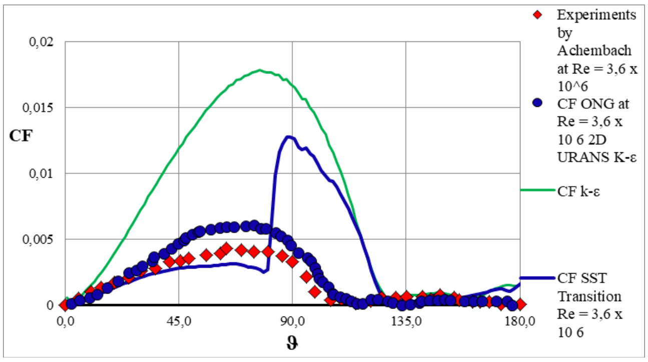


Figure 14. Skin friction factor comparison at $Re=3.6x10^6$

Table 4. Skin friction coefficient comparison

| Study case | $\theta_s$ $Re=1\times10^6$ | $\Theta_b$ $Re=1\times10^6$ | $\theta_s$ $Re=3.6\times10^6$ | $\Theta_t$ $Re=3.6\times10^6$ |
|---|---|---|---|---|
| URANS k-ε | 122.81 | - | 128.91 | - |
| URANS (Trans. γ-θ) | 127.39 | 104.51 | 128.91 | 67.91 |
| Ong et al. URANS k-ε [20] | 110.88 | - | 114 | - |
| Zhang et al. URANS k-ε [28] | 123.5 | - | - | - |
| Ref [25] | 135 | 105 | 115 | 65 |

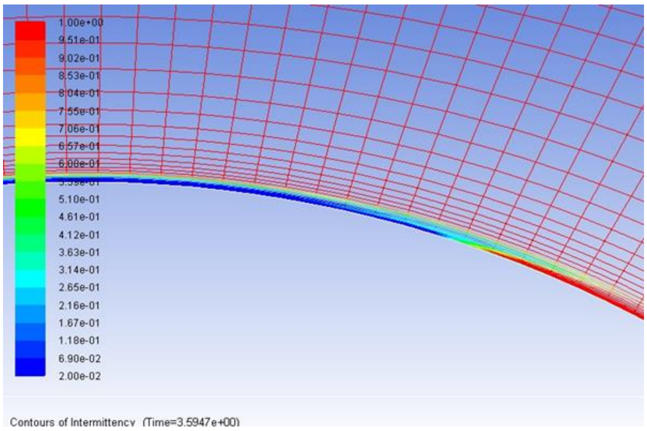


Figure 15. Intermittency function to show the laminar bubble at the wall

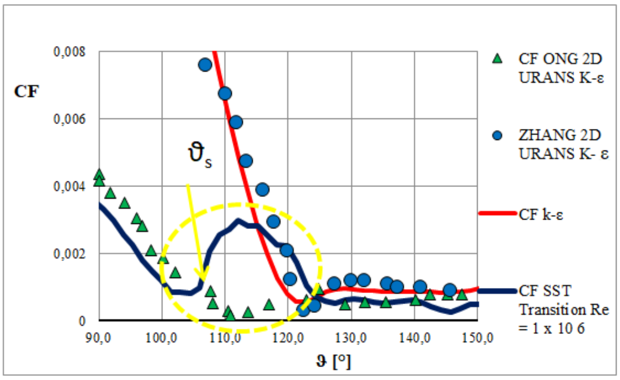


Figure 16. Friction coefficient distributions: recirculating bubble at Re=1x10$^6$

## 4 A method to evaluate the length of the recirculation bubble downstream the cylinder

In this section the proposed methodology to quantify the recirculating area downstream of a bluff body is described. From the values of Table 5 it can be observed that increasing the Reynolds number (with the free stream velocity $U_\infty$) the shedding frequency increases. The centerline of the cylinder in the wake is considered, called Wake Centre Line. The shedding phenomenon is periodic so the recirculation bubble behind the cylinder changes at every time step. After the analysis of the velocity contour frames it has been observed that the influenced zone behind the cylinder extends for a length of about two diameters. The velocity profile in this region on the centerline is investigated.

Table 5. Frequency and Strouhal comparison

| Study case | f [Hz] Re=1×10⁶ | St Re=1×10⁶ | f [Hz] Re=3.6×10⁶ | St Re=3.6×10⁶ |
|---|---|---|---|---|
| URANS k-ε | 96.824 | 0.2635 | 265.958 | 0.2011 |

The recirculation zone end point is identified as the first point where the outside fluid flows and crosses through the central axle i.e. the Wake Centre Line, as discussed in ref. 14. A series of monitor points (numerical probes) have been positioned on the Wake Center Axis and the following velocity ratio is monitored:

$$\Psi = \frac{\bar{u}_x}{U_\infty} \tag{20}$$

where the time averaged local axial velocity is introduced at the numerator.

A negative value means reversed flow thus a recirculation zone. The dimensional recirculating bubble in axial direction x was time averaged as in Figure 17:

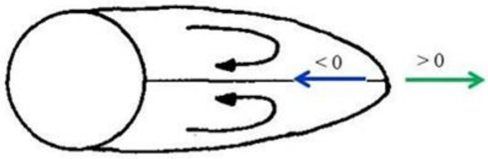


Figure 17. Schematic of steady recirculating bubble

The axis starts from the cylinder center and the non-dimensional coordinate x/D is used. The point where the axial velocity is zero ($u_x$= 0) can be obtained and this is considered the end point of the recirculating bubble. In order to locate the above point the centerline was discretized with an appropriate spatial step Δx. The monitored values of velocity ratio are time-averaged of a period of 10T of the shedding frequency (according to the Strouhal number). Twenty probes equally spaced (Δx= 0.02 [m]) have been inserted on the Wake Center Line in a length of 2D from the cylinder as shown in Figure 18.

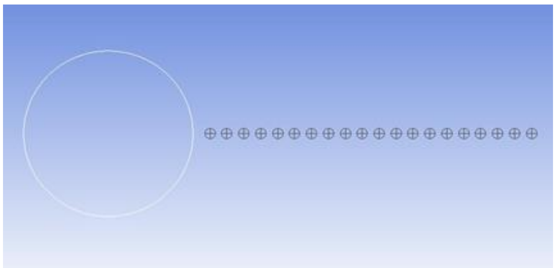

Figure 18. First investigation with 20 equally spaced probes

The velocity ratio distributions of Figure 19 and Figure 20 are obtained for the two values of Re considered. For Re=1×10$^6$ the spatial discretization has been reduced to Δx = 0,01 [m]. Figure 21 shows the comparison of the two investigation sets and confirms that the original discretization was adequate to accurately reconstruct the velocity ratio along the centerline.

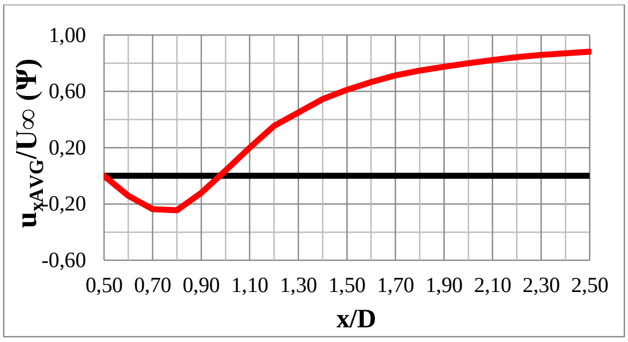


Figure 19. Axial velocity ratio Ψ along wake centerline at Re=1×10$^6$

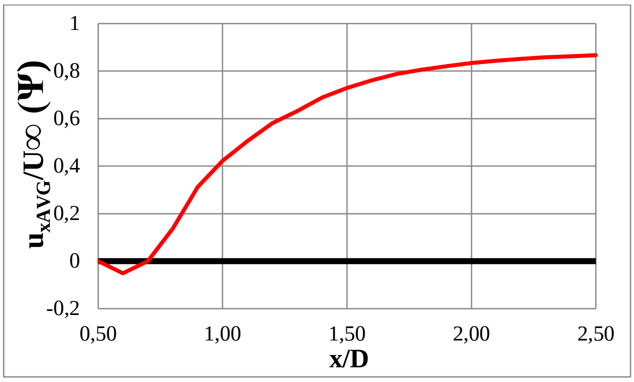


Figure 20. Axial velocity ratio Ψ along wake centerline at Re = 3.6 $\times 10^6$

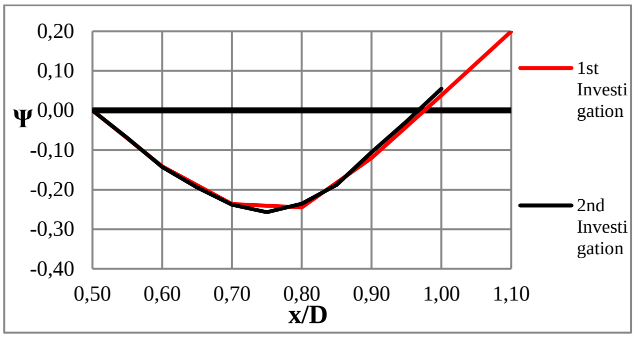


Figure 21. Axial velocity ratio Ψ along wake centerline at Re=$1\times10^6$ – detail of monitor points distribution

The above diagrams can highlight the correlation between Reynolds number (free stream velocity) recirculation length and shedding frequency [4]: an increase in Re gives higher shedding frequency and shorter recirculation zone. In Figure 20 at Re=$3.6\times10^6$ the recirculation zone is extinguished from x/D = 0.7 while at Re=$1\times10^6$ the recirculation is closed at x/D=0.97 (Figure 21). A second investigation for case Re=$3,6\times10^6$ with a higher number of probes (higher resolution) has been performed and the results are shown in Figure 22.

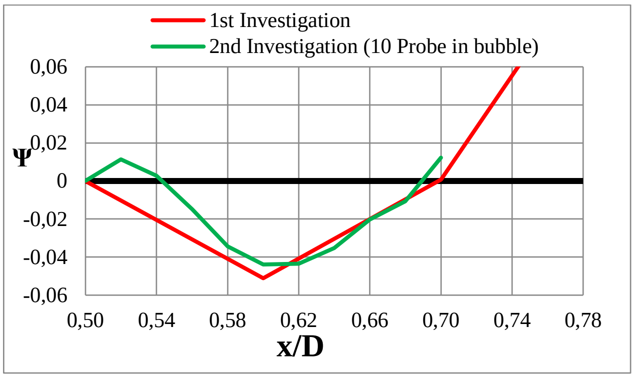


Figure 22. Comparison of Ψ between two monitor points distributions at Re=$3,6\times10^6$ along the wake centerline

In this case the velocity distribution behind the cylinder highlights a recirculation bubble at the cylinder wall detected by the first crossing of zero value at about x/D=0.54. This suggested the presence of a second vortex connected to the main vortex shed. To have a deeper insight it was decided to set 20 probes along the wake center line between x/D = 0.5 and x/D=0.54.

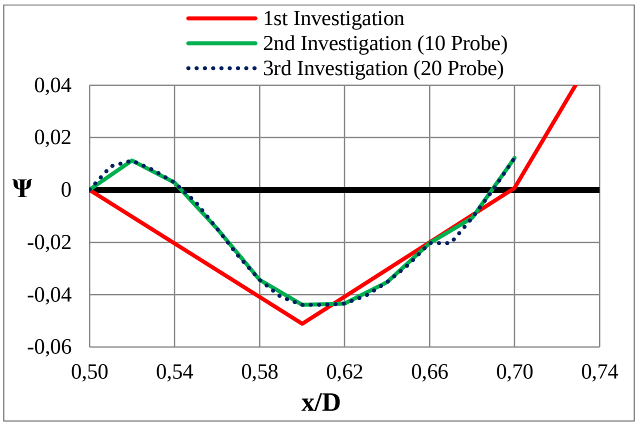


Figure 23. Comparison of Ψ between 1st, 2nd and 3rd investigations probes sets at Re=$3,6\times10^6$

In Figure 23 the results from the refined probes line (3rd investigation) is compared to the previous analysis and it confirms that the distribution criteria previously set is adequate to capture also this small feature. The main recirculation averaged from the unsteady analysis is closed at x/D=0,69. From the above velocity averaged distribution along the cylinder axis it can be argued that the additional small vortices are generated by the shear layer from the opposite main vortices shed from the lateral walls of the cylinder. The vorticity contours of Figure 24 help to support the above physical interpretation of the presence of a couple of counter-rotating vortex pairs: the main external vortices and the inner small pair.

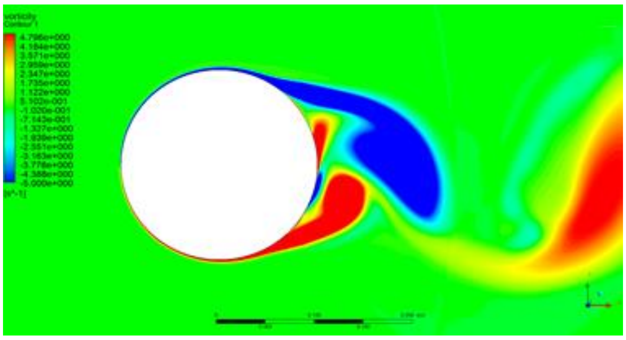

Figure 24. Contra-rotating vortex pairs

In Figure 25 the velocity ratio distributions for the two Reynolds considered are compared to have a direct view of the difference in recirculation zone length with Re that correlates to the shedding frequency.

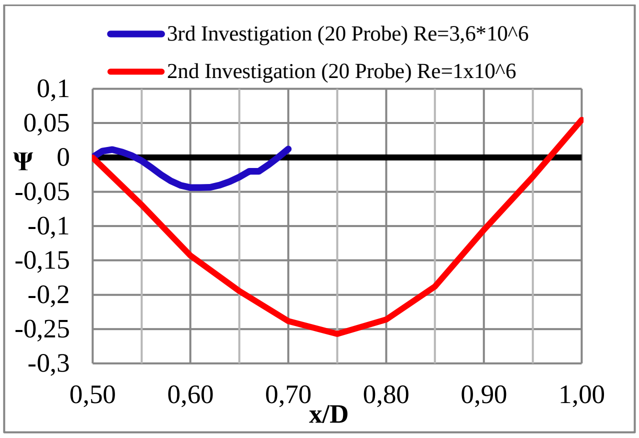


Figure 25. Comparison of the velocity ratio distributions for the two Reynolds cases

In Table 6 the variation of the vortex release frequency with the Reynolds number is reported together with the above recirculation lengths. Higher Re corresponds to higher frequency and shorter recirculation length as defined above.

Table 6. Dimensionless Recirculation length comparison.

| Study case | Re | f [Hz] | St | x/D (Recirculation length) |
|---|---|---|---|---|
| 2D URANS k-ε | $1\times10^6$ | 96.82 | 0.2635 | 0.967 |
| 2D URANS k-ε | $3.6\times10^6$ | 265.9 | 0.2011 | 0.690 |

The frequency and the recirculating length are inversely proportional due to the interaction of shear layers outside the wake; the separation angle increases with Re (Table 4) and the separated zone intensity is increased but the wake extension is reduced.

## 5 Application of the recirculation length method to an airfoil with Gurney flap at high Reynolds number

The recirculation length criterion to investigate the vortex shedding is applied to the engineering case of an aerodynamic profile with a Gurney flap to test the correlation between vortex shedding frequency and recirculation length already observed for the cylinder case. The same case has been extensively investigated using CFD [9] and the experience gained has been used to perform the CFD simulations of the present work. The same reference configuration from [9] is used and the case of Gurney Flap height 2.9% of C in ground effect with h/C=0.448 is considered. The computational domain is a rectangle that extends 2.5C from the leading edge, 11C from the trailing edge and 6C in the upper and lower sides. A hybrid multiblock grid formed by tetrahedrons (outer zone) and structured grid (inner zone close to profile) is generated with element clustering at the viscous walls to obtain y+ close to one. A total 2D mesh of 80 kCells is obtained and a zoomed view is shown in Figure 26. The mesh has been adopted for the simulations after a thorough grid sensitivity analysis [9].

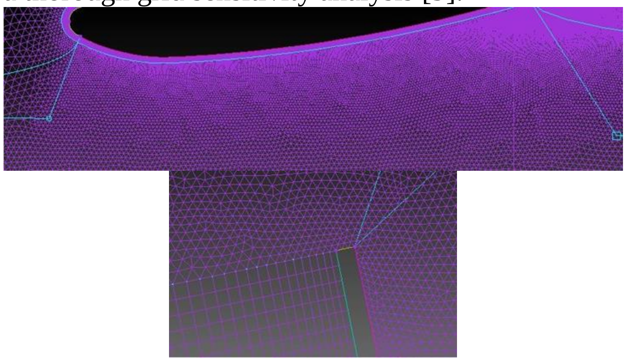

Figure 26. Mesh details of Gurney Flap domain

At the inlet boundary the velocity is fixed together with a turbulence intensity equal to 0.2%. Two simulations are performed: Re=$0.462x10^6$ (corresponding to an incoming velocity U=7 m/s) and Re=$1x10^6$ (U=15.2 m/s). At the outlet the reference pressure is set, the ground is a viscous wall moving at the incoming flow speed. The upper boundary is set as an inviscid slip wall. The k-ε turbulence model and a timestep $\Delta t$ = 2.118 $x10^{-4}[s]$ are selected. The results are validated against reference data [30, 31]. All the selected cases give rise to a vortex shedding phenomenon and in the simulations the flow begins to oscillate after 1.7 [s] at Re=$0.462x10^6$ and after 0.7 [s] at Re=$1x10^6$. In Figure 27, 28, 29, 30 the contours of vorticity, velocity and eddy viscosity show the Von Karman vortex shedding behind the airfoil with the Gurney flap at the two operating conditions.

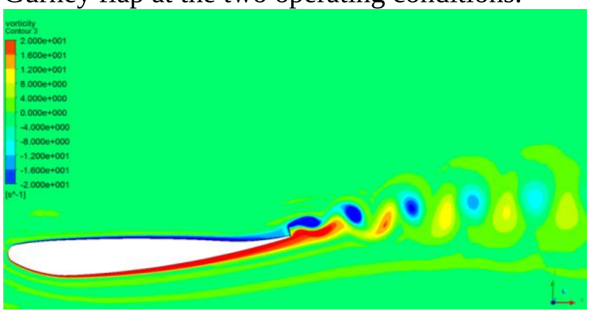

Figure 27. Vorticity Contour showing Von Karman street vortex at Re=$0.462x10^6$

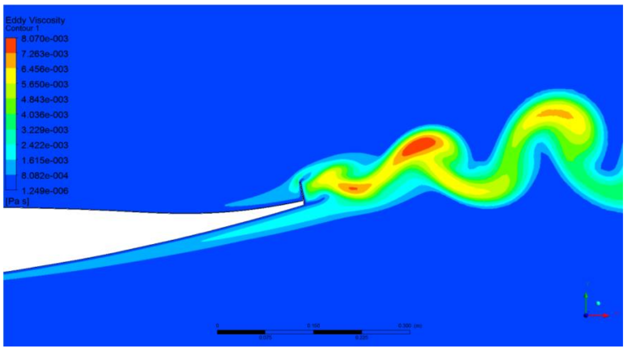

Figure 28. Eddy Viscosity Contour showing Von Karman street vortex at Re=$0.462x10^6$

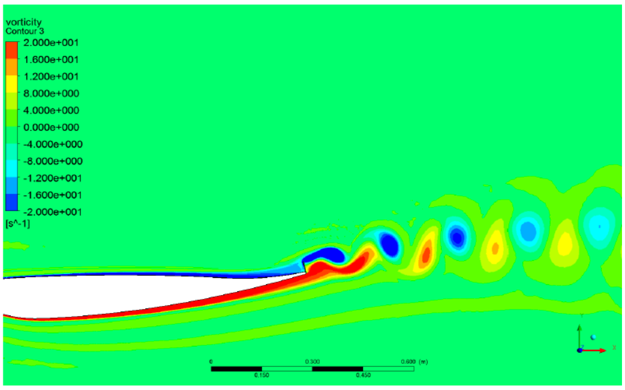

Figure 29. Vorticity Contour showing Von Karman street vortex at Re=$1x10^6$

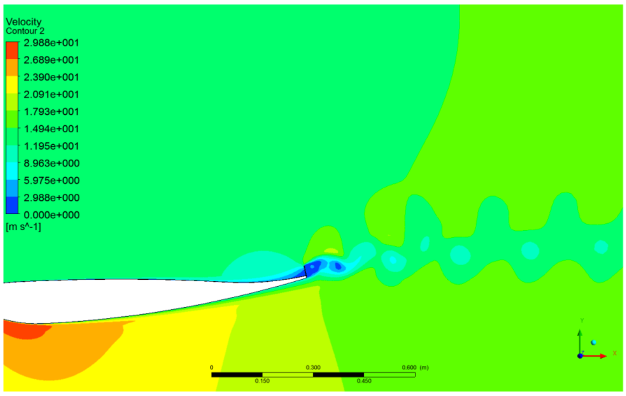

Figure 30. Velocity Contour showing Von Karman street vortex at Re=$1x10^6$

To determine the Strouhal number of the shedding the selected characteristic size for the Gurney is d from Eq. (21):

$$d = 2.9\%C + h_t \quad (21)$$

where $h_t$ is the trailing edge thickness.

Table 7. Lift Coefficient results comparison

| Study case | Re | $C_L$ |
|---|---|---|
| URANS k-ε | $0.462×10^6$ | 1.876 |
| DES Unsteady [9] | $0.462×10^6$ | 1.801 |
| Spalart Allmaras steady [9] | $0.462×10^6$ | 1.856 |
| SST steady [9] | $0.462×10^6$ | 1.742 |
| Zerihan exp. [31] | $0.462×10^6$ | 1.557 |
| URANS k-ε | $1×10^6$ | 1.919 |

Table 8. Strouhal number results comparison

| Study case | Re | T [s] | f [Hz] | St |
|---|---|---|---|---|
| URANS k-ε | $0.462×10^6$ | 0.341 | 29.326 | 0.152 |
| DES Unsteady [9] | $0.462×10^6$ | - | - | 0.156 |
| Zerihan exp. [31] | $0.462×10^6$ | - | - | 0.178 |
| Jeffrey | - | - | - | 0.08 – 0.15 |
| URANS k-ε | $1×10^6$ | 0.0150 | 66.499 | 0.159 |

The lift coefficient is considered:

$$C_L = \frac{L}{\frac{1}{2}\rho A U^2} \quad (22)$$

and Table 7 shows the values of $C_L$ compared to the reference data. All the numerical values overestimate the experimental value and, as discussed in [9,30,31] this is due to the fact that all simulations are exactly 2D while the experimental data are obtained at midspan of a 3D wing. The Gurney flap introduces a pressure difference at the trailing edge, which leads to increased circulation and, due to the Helmholtz theorem, to increased lift. Moreover, in ground effect, the flow between the ground and the profile suction side is accelerated giving a higher lift (downforce) with respect to the same profile in freestream (far from ground).

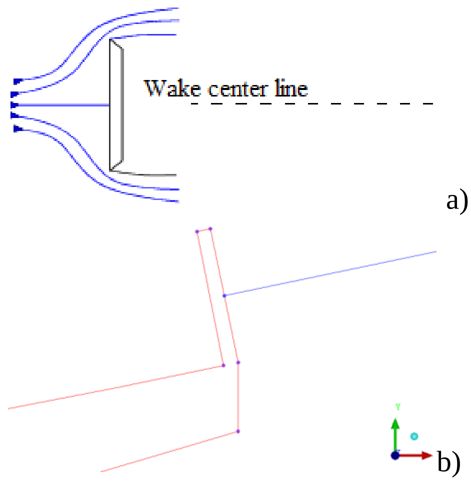


Figure 31. Reference centerline in the wake. a) flat plate, b) Gurney flap

### 5.1 Skin Friction Coefficient

The methodology developed for the cylinder is applied to the case of the Gurney flap. The proper reference line for monitoring points set must be defined. This is obtained with the case of a flat plate perpendicular to the incoming flow in mind (Figure 31a); the equivalent of the flat plate is the flap as in Figure 31b where a detail of the trailing edge with flap is reported together with the sketch of the reference line. From the simulations it has been observed that the real recirculation zone, including the shedding of the first vortex, extends for about one-third of the chord along the above reference direction. Forty monitoring points have been set in centerline with three different levels of uniform spacing with a higher resolution in the first part behind the flap as sketched in Figure 32.

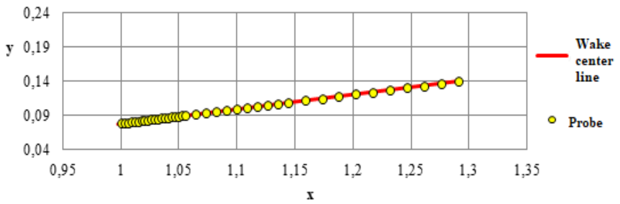


Figure 32. Monitoring points in the centerline for Gurney flap

The velocity components and magnitude are monitored in the above numerical probes. The velocity components are then projected to obtain the velocity components along the centerline and perpendicular to it. As for the cylinder case the instantaneous values for each probe are averaged over ten periods of the oscillation for both Reynolds number considered. The velocity ratio Ψ is introduced as the ratio between the local velocity magnitude in the centerline direction (δ) and the upstream freestream flow velocity:

$$\Psi = \frac{\bar{u}_{\delta}}{U_{\infty}} \tag{23}$$

The investigations for the two Reynolds numbers were performed collecting the data of the probes in ten periods of oscillations corresponding to 0.35 [s] ($Re=0.462x10^6$) and 0.16 [s] ($Re=1x10^6$) of the unsteady flow evolution. A single period T corresponds to the characteristic period of the vortex release. Ten periods have been chosen to average the terms of the velocity ratio Ψ, in order to have a statistic simulation period and to eliminate any numerical disturbances that might occur, as in the cylinder case. Table 9 shows the results of the simulations for the shedding frequency, Strouhal number and coordinate along the centerline where the recirculation zone ends.

Table 9. Recirculation length results comparison

| Study case | Re | f [Hz] | St | x/C |
|---|---|---|---|---|
| 2D URANS k-ε | $0.426\times10^6$ | 29.3 | 0.152 | 1.072 |
| 2D URANS k-ε | $1\times10^6$ | 66.5 | 0.159 | 1.062 |

The above coordinates are obtained from the distribution of the velocity ratio along the centerline as in Figure 33; they correspond to the condition $u_\delta$= 0. The x coordinate origin is at the profile leading edge, therefore, the recirculation zone ends at a distance equal to about 7%C of the chord at $Re=0.462x10^6$ and at a distance of about 6.2%C of the chord downstream of the Gurney flap for $Re=1x10^6$.

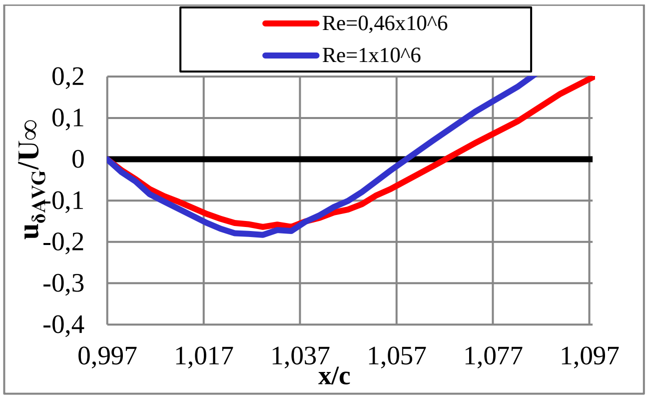


Figure 33. Velocity ratio distributions along the wake centerline; recirculation length comparison

The results in Table 9 confirm the correlation between the shedding frequency and the recirculation length as defined above.

A higher frequency has a shorter recirculation length and vice versa. In fact from Figure 33, with an increased Reynolds number (blue line) the recirculation length (the ratio in eq. (23)) cuts the abscissa axis before.

The flow mechanisms behind the vortex shedding and its frequency are due to the interaction of the shear layers outside the wake [9,30-34] and with Reynolds number increase their interaction increases with higher strength.

The Gurney flap case with h/C = 0.448 has been widely documented both numerically [9] and experimentally using PIV techniques [30,31].

The velocity ratio profile along the wake centerline is superimposed in Figure 34 to the vorticity contours to graphically show the connection of the vortex shedding with the recirculation length previously discussed.

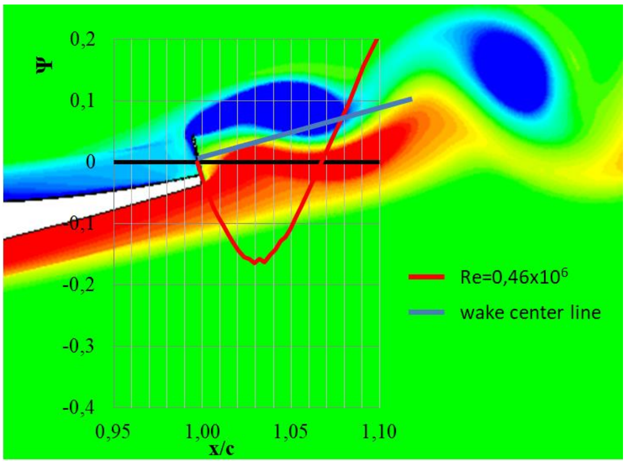


Figure 34. Overlapping for velocity ratio distribution along the wake centerline and the vorticity contours

## 6 Conclusion

The modeling of the turbulent flows continues to represent a crucial problem of the computational fluid dynamic and classical physics. In this work a methodology for the prediction of the recirculation length of the unsteady wake from a bluff body has been developed. Two different application cases have been adopted: the circular cylinder and the profile with Gurney flap. Different influence parameters for the vortex shedding phenomenon have been analyzed. This phenomenon has been carefully predicted by 2D RANS model also in supercritical regime, by highlighting the complex wall flow structure. This methodology has been validated by the experimental measures. The recirculation length of the average wake from the unsteady simulations has been used to correlate with the shedding frequency. The quantitative correlation of higher recirculation length with lower shedding frequency (and vice versa) has been confirmed for both application cases at different operating conditions. This methodology can give an engineering support to more practical cases, as in the building sector. The recirculation length criterion can be extended to 3D cases with the introduction of a numerical probes matrix instead of the linear probe distribution.

*Nomenclature:*

| | |
|---|---|
| A | Reference area |
| C | Chord |
| $C_D$ | Drag coefficient |
| $C_L$ | Lift coefficient |
| $C_p$ | Pressure coefficient |
| $Cp_b$ | Base pressure coefficient |
| d | Gurney flap characteristic dimension |
| D | Cylinder diameter |
| $D_R$ | Drag force |
| f | Vortex Shedding frequency |
| k | Turbulent kinetic energy |
| L | Lift force |
| p | Pressure |
| $p_\infty$ | Reference pressure |
| Re | Reynolds number |
| S | Strain rate magnitude |
| St | Strouhal number |
| t | Timestep |
| T | Period |
| $u_{avg}$ | Average x-velocity |
| $\bar{u}_\delta$ | Average Gurney wake velocity |
| U | Velocity (magnitude) |
| $u_x$ | Velocity along x-axis |
| $u_y$ | Velocity along x-axis |
| $U_\infty$ | Freestream velocity |
| x | Horizontal position |
| $y^+$ | Wall non-dimensional distance |
| $\gamma$ | Intermittency |
| $\Gamma$ | Circulation |
| $\delta$ | Wake direction at Gurney flap trailing edge |
| $\varepsilon$ | Rate of dissipation of turbulent kinetic energy |
| $\vartheta$ | Angular position in the cylinder from stagnation point |
| $\mu$ | Dynamic viscosity |
| $\rho$ | Density |
| $\tau_w$ | Wall shear stress |
| $\Psi$ | Dimensionless recirculation length |
| $\omega$ | Specific rate of k dissipation |
| $\Omega$ | Dimensionless vorticity |

*Subscripts*

| | |
|---|---|
| b | Separation |
| s | Starting recirculation bubble point |
| t | Transition from laminar to turbulent boundary layer |

*References:*

[1]. Strouhal, V. Ueber eine besondere Art der Tonerregung (On an unusual sort of sound excitation). Annalen der Physik und Chemie, 3rd series 1878, Vol. 5 (10), pp. 216–251.

[2]. Rayleigh, L. The Principle of Similitude. Nature 1915, Vol. 95, pp. 66-68.

[3]. Kármán, Th. von; Rubach, H. (1912). Über den Mechanismus des Flüssigkeits - und Luftwiderstandes [On the mechanism of fluid and air resistance]. Physikalische Zeitschrift 1912, Vol. 13, pp. 49–59.

[4]. Gerrard, J.H. The Mechanics of the Formation Region of Vortices Behind Bluff Bodies. Journal of Fluid Mechanics 1966, Vol. 25, part 2, pp. 403-413

[5]. Bloor, M.S. The Transition to turbulence in the Wake of a Circular Cylinder. Journal of Fluid Mechanics 1964, Vol. 19, p.290.

[6]. Schewe, G. On the Force Fluctuations Acting on a Cylinder in Crossflow from Subcritical up to Transcritical Reynolds Number. Journal of Fluids Mechanics 1983, Vol. 133, pp. 265-285.

[7]. Williamson, C.H.K. Vortex Dynamics in the Cylinder Wake. Annual Reviews Fluid Mechanics 1996, Vol. 28, pp. 477-539.

[8]. Roshko, A. On the Drag and Shedding Frequency of Dwo-Dimensional Bluff Bodies. 1954, NACA TN no. 3169.

[9]. Cravero C., Aerodynamic performance prediction of a profile in ground effect with and without a Gurney flap, ASME J. of Fluids Engineering, doi:10.1115/1.4035137, March 2017, Vol. 139, pag. 031105-1-031105-15;

[10].Jeffrey L. D. An Investigation into the Aerodynamics of Gurney Flaps. Ph.D Dissertation, University of Southampton, UK, June 1998.

[11].Liebeck, R.H. Design of subsonic airfoils for high lift. Journal of Aircract 1978, Vol. 15, No. 9, pp. 547-561.

[12].Jeffrey, D. Aerodynamics of Gurney Flaps on a Single-Element High-Lift Wing. Journal of Aircraft 2000, Vol. 37, No. 2.

[13].Cravero, C.; De Domenico, D.; Leutcha, P.J.; Marsano, D. Strategies for the numerical modelling of regenerative pre-heating systems for recycled glass raw material. Math. Model. Eng. Probl. 2019, Vol. 6, pp. 324–332.

[14].Zhang, Y.; Vanierschot, M. Modeling capabilities of unsteady RANS for the simulation of turbulent swirling flow in an annular bluff-body combustor geometry. Applied Mathematical Modelling 2021, Vol. 89, Part 2, pp. 1140-1154.

[15].Cravero, C.; Marsano, D. Numerical prediction of tonal noise in centrifugal blowers. Turbo Expo 2018: Turbomachinery Technical Conference & Exposition, June 11-15, 2018, Oslo, Norway, ASME Paper GT2018-75243.

[16].Benim, A.C.; Pasquotto, E.; Suh, S.H. Modeling turbulent flow past a circular cylinder by RANS, URANS, LES and DES. Progress Comput. Fluid Dyn. Int. J. 2008, Vol. 8, pp. 299–307.

[17].Liuliu, S.; Yang, G.; Yao, S. Large eddy simulation of flow past a square cylinder with rounded leading corners: A comparison of 2D and 3D approaches. J. Mech. Sci. Technol. 2018, Vol. 32, pp. 2671–2680.

[18].Launder, B.E.; Spalding, D.B. Mathematical models of turbulence. Accademic press 1972, London.

[19].Rodi, W. Turbulence models and their application in hydraulics. A state-of-the-art review. IAHR Monograph Series, 3RD edition, Rotterdam, Netherlands.

[20].Ong, M.C.; Utnes, T.; Holmedal, L.E.; Myrhaug, D. Numerical simulation of flow around a smooth circular cylinder at high Reynolds number. Marine structures 2009, Vol. 22, pp. 142-153.

[21].Ansys Fluent Theory Guide. ANSYS Inc.

[22].Roshko, A. Experiments on the flow past a circular cylinder at very high Reynolds number. Journal of Fluid Mechanics 1961, Vol. 10, Issue 3, pp. 345-356.

[23].Wieselsberger, C. Results of aerodynamic research at Gottingen (in German), II Lieferung, 1923.

[24].Delaney, N.K.; Sorensen, N.E. Low speed drag of cylinders of various shapes. NACA TN 3038, 1953.

[25].Achenbach, E. Distribution of local pressure and skin fiction around a circular cylinder in cross-flow up to Re = 5×106. Journal of Fluid Mechanics 1968, Vol. 34, part 4, pp. 625-639.

[26].Relf, E.F; Simmons, L.F. The frequency of eddies generated by motion of circular cylinders at cross flow at very high Reynolds numbers. Aero. Res. Counc., 1924, Lond, Rep. Mem. P.917.

[27].Warschauer, K.A., Leene, J.A. Experiments on mean and fluctuating pressures of circular cylinders at cross flow at very high Reynolds numbers. In: Proceeding of the international conference on wind effects on builidings and structures, 1971, pp. 305-15, Tokyo, Japan.

[28].Zhang, X.; Li, Z.Y.; Fu, S.; Ong, M.C.; Chen, Y. Study of the Flow Around a Cylinder from the Subcritical to Supercritical Regimes. Ocean Systems Engineering 2014, Vol. 4, No. 3, pp. 185-200.

[29].Rodi, W. On the simulation of turbulent flow past bluff bodies. Journal of Wind engineering and Industrial Aerodynamics 1993, Vol. 46-47, pp. 3-19.

[30].Zerihan, J.; Zhang, X. Aerodynamics of Gurney Flaps on a Wing in Ground Effect. AIAA Journal 2001, Vol. 39, No. 5.

[31].Zerihan, J.; Zhang, X. Aerodynamics of a Single Element Wing in Ground Effect. AIAA Paper 2000-0650, 2000.
[32].Ferziger, J.H. The physics and simulation in turbulence - Introduction to turbulence modelling. VKI Lectures Series 2004-06, Sanford University, USA, 2004.
[33].Hielder, H.E. Coherent structures in a turbulent flows. Prog. Aerospace Sci. 1988, Vol. 25, pp. 231-269.
[34].Brown, G.L.; Roshko, A. On Density Effects and Large Structure of Turbulent Mixing Layers. Journal of Fluid Mechanics 1974, Vol. 64, pp. 775.

## Contribution of individual authors to the creation of a scientific article (ghostwriting policy)

The authors have contributed in equal part to the development of the research work and to the editing and preparation of the manuscript